PROCEEDINGS, 51st Workshop on Geothermal Reservoir Engineering
Stanford University, Stanford, California, February 9-11, 2026
SGP-TR-230

Unpropped but Unignored: Optimizing Perforation Strategy and Geothermal Efficiency through Fracture Conductivity Profiling

Ali Zidane*, Brandon Hobbs, Xiaowei Weng, Safdar Abbas, Abdul Muqtadir Khan, Olga Kresse

Schlumberger, Sugar Land, TX, USA

amzidane@slb.com

Keywords: Arch Region, Fracture Conductivity, Perforation Strategy Optimization, Enhanced Geothermal Systems (EGS), Numerical Simulation

ABSTRACT

Unpropped fracture segments—often referred to as arch regions or residual openings—play a critical yet underexplored role in subsurface flow dynamics. While conventional hydraulic fracturing models focus primarily on propped zones, emerging evidence suggests that even low conductivity unpropped regions can significantly influence fluid transport and energy recovery. This study presents a numerical investigation into the impact of unpropped channel conductivity on perforation placement optimization and thermal performance in Enhanced Geothermal Systems (EGS).

Using a custom in-house simulator, we model a series of fracture configurations with varying unpropped channel heights and permeability contrasts. Results demonstrate that the presence and geometry of unpropped channels alter flow pathways and temperature evolution at the production well over time. Comparative analysis against homogeneous fracture models reveals substantial deviations in system behavior, underscoring the importance of incorporating conductivity heterogeneity into design and simulation workflows.

This work bridges a critical gap in current modeling practices by quantifying the operational significance of unpropped fracture zones. It offers a foundation for more accurate perforating and doublet strategies leading to improved EGS system efficiency, while opening avenues for future integration with real-time monitoring and adaptive control technologies.

1. INTRODUCTION

Enhanced Geothermal Systems (EGS) represent a highly promising avenue for sustainable energy resources, with vast untapped potential (Lund et al., 2011; Bertani, 2012; Jung, 2013). Unlike conventional hydrothermal resources, EGS is not constrained by the presence of naturally high-permeability formations or abundant groundwater. Instead, it relies on engineering interventions—such as hydraulic fracturing to create or enhance fracture networks within low-permeability crystalline rock (Tenma et al., 2008; Brown, 2009).

Fluid circulation within an EGS reservoir may be governed either by flow through a dominant fracture (Brown, 2009; Llanos et al., 2015), or by movement across a complex, interconnected fracture network (Koh et al., 2011; Genter et al., 2013). In both scenarios, the spatial and temporal evolution of flow paths along individual fractures—and the efficiency of heat exchange between the circulating fluid and surrounding rock—are critical determinants of thermal output and overall system performance.

Hydraulic stimulation remains a foundational technique in subsurface energy extraction in EGS. However, achieving consistent fracture conductivity continues to be a major challenge. While conventional models often assume uniformly propped fractures, field observations and recent advances reveal that unpropped segments—commonly referred to as "arch regions" or "residual openings"—can significantly influence both fluid movement and thermal transport. During hydraulic fracturing, proppant often settles into a bank at the base of the fracture. As hydraulic pressure is gradually released, the overlying unpropped section of the fracture begins to close partially, forming an arched zone above the proppant bank. The dimensions of this arch—its width and height—shrink as fluid pressure declines, and the effect is more pronounced in formations with low proppant concentrations or high compressibility.

This arched region, despite being unpropped, can exhibit high conductivity and act as a preferential flow pathway. Its presence plays a critical role in shaping fluid transport dynamics and significantly affects the overall transmissivity of the fracture system (Wang and Elsworth 2018). Palisch et al. (2010) describes several plausible proppant arrangements that may develop during slickwater fracturing, each with distinct implications for fracture geometry and conductivity. One scenario involves proppant settling at the base of a relatively planar vertical fracture, where the unsupported upper section may partially close post-treatment, forming an arched void space. This configuration is likely to occur in simpler fracture systems or along primary flow paths. Another scenario involves more complex fracture geometries, where proppant becomes trapped at irregularities along the fracture face, resulting in a network of arches, pinch points, and voids interspersed with proppant beds. A third possibility includes partial-monolayer deposition, which may arise when buoyant proppants or narrow fissures restrict full packing. These configurations underscore the variability of proppant placement and its influence on fracture conductivity and fluid transport behavior. As result, during proppant injection, complete coverage of the fracture domain is rarely achieved, if not impossible, as proppant tends to settle and accumulate unevenly within the fracture (Shao et al., 2025; Wu, 2017).

In EGS, heat is extracted by circulating fluid through fractures, transferring thermal energy from the surrounding rock to production wells. Crucially, only the portions of the fracture that actively carry flow contribute to effective heat exchange. Ideally, flow should be distributed across a broad area of the fracture surface to maximize thermal contact. Previous work by Samuel et al. (2008) introduced a dynamic

proppant placement system that uses real-time sensor feedback to form proppant clusters with open channels between them, enhancing flow efficiency from reservoir to wellbore. Similarly, Alimahomed et al. (2021) proposed a dual-pack proppant strategy that improves conductivity in previously unpropped upper fracture sections, demonstrating that even low-conductivity zones can substantially boost hydrocarbon production. Zhou et al. (2019) investigated the impact of unpropped fracture conductivity in huff-n-puff operations, showing that minimally conductive regions still contribute meaningfully to overall flow behavior. Zhang et al. (2018) examined the transmissibility of the arch region and concluded that its hydraulic behavior warrants deeper consideration. The work by Liu et al. (2018) provides a detailed geomechanical and flow simulation analysis of partially propped fractures, highlighting the critical role of uneven proppant distribution in shaping fracture closure behavior and fluid transport. Their findings identify three distinct zones within a partially propped fracture: a propped region, an unpropped region, and an arch. The residual opening, formed above the proppant pack during pressure decline, acts as a high-conductivity pathway that can significantly influence gas production and water recovery. The study emphasizes that neglecting the geometry and closure dynamics of these residual openings may lead to inaccurate predictions of well performance and inefficient operational strategies. Warpinski (2009) emphasized the mechanical significance of the arch zone as a high-conductivity pathway, although his work did not address fluid or thermal transport.

Despite these insights, the geothermal domain has yet to fully integrate the dynamics of unpropped fracture segments into system design and optimization. This paper addresses that gap by presenting a comprehensive numerical investigation into the role of unpropped channels in EGS performance. Using our custom-built simulator, we evaluate how these residual openings influence well placement strategies and subsurface thermal efficiency. Our findings reveal that unpropped zones are not merely passive features but active contributors to geothermal system behavior, offering new avenues for performance enhancement and predictive control.

2. MATHEMATICAL MODEL

The temperature distribution within the fracture is influenced by convective heat transport along the fracture axis, as well as thermal exchange with the surrounding rock through both fracture surfaces. The corresponding equation describing fluid temperature behavior in the fracture is given by:

$$\rho_f c_f \frac{\partial T_f}{\partial t} + \nabla\left(\rho_f c_f \boldsymbol{q} T_f\right) = Q_f(x,y,z) + Q_i \delta_{(x_i,y_i,z_i)} \tag{1}$$

where c_f is the specific heat of fluid, ρ_f is the fluid density, T_f is the fluid temperature, $\boldsymbol{q}$ is the specific discharge (Zimmerman et al, 1991), Q_f is the heat transfer rate between the fracture and the rock matrix, $\delta_{(\boldsymbol{x_i},\boldsymbol{y_i},\boldsymbol{z_i})/(\boldsymbol{x_p},\boldsymbol{y_p},\boldsymbol{z_p})}$ the Dirac delta function and $(\boldsymbol{x_i},\boldsymbol{y_i},\boldsymbol{z_i})/(\boldsymbol{x_p},\boldsymbol{y_p},\boldsymbol{z_p})$ the coordinates of injection/production wells, and Q_i is the heat injected into the fracture at the location of the injection wells.

Heat conduction is the predominant mode of transport in low-permeability geothermal reservoir matrices, and can be mathematically represented as:

$$\begin{cases} \rho_r c_r \dfrac{\partial T_r}{\partial t} - \nabla.(k_r \nabla T_r) = Q_m(x,y,z) \\ Q_m = -Q_f \end{cases} \tag{2}$$

where ρ_r is the rock density, c_r is the rock heat capacity, $T_r$is the rock temperature, k_r is the rock thermal conductivity, and Q_m is the heat exchange with the fracture (with $Q_f + Q_m = 0$).

3. NUMERICAL SIMULATIONS

This section presents a series of numerical simulations designed to highlight the significance of the proposed modeling framework. The study considers a fracture measuring 300 × 200 m² with a thickness of 1 mm, embedded within a larger matrix domain of 100 × 500 × 400 m³ (Figure 1). Multiple simulation scenarios are explored to assess the impact of a high-conductivity channel on thermal output, and by extension, the efficiency of Enhanced Geothermal Systems (EGS). The channel height is varied systematically from 10% to 90% of the total fracture height. Figure 2 illustrates the configuration for the 10% case, where the fracture is partitioned into two distinct conductive zones: a propped region with defined permeability, and an overlying high-conductivity channel of variable height. The channel is assumed to be 1000 times more conductive than the propped region, though higher permeability ratios are plausible. Two injection rate values are considered: 250 m^3/day and 500 m^3/day. Additionally, the simulations examine various injector and producer placements at the bottom, middle, and top of the fracture, enabling an evaluation of well placement strategies for optimizing EGS performance. In all simulations the injector is at the left side of the fracture and producer is at the right side of the fracture. Each scenario is benchmarked against a base case featuring homogeneous fracture permeability, i.e., without a high-conductivity channel. Simulation time for all cases is 10 years.

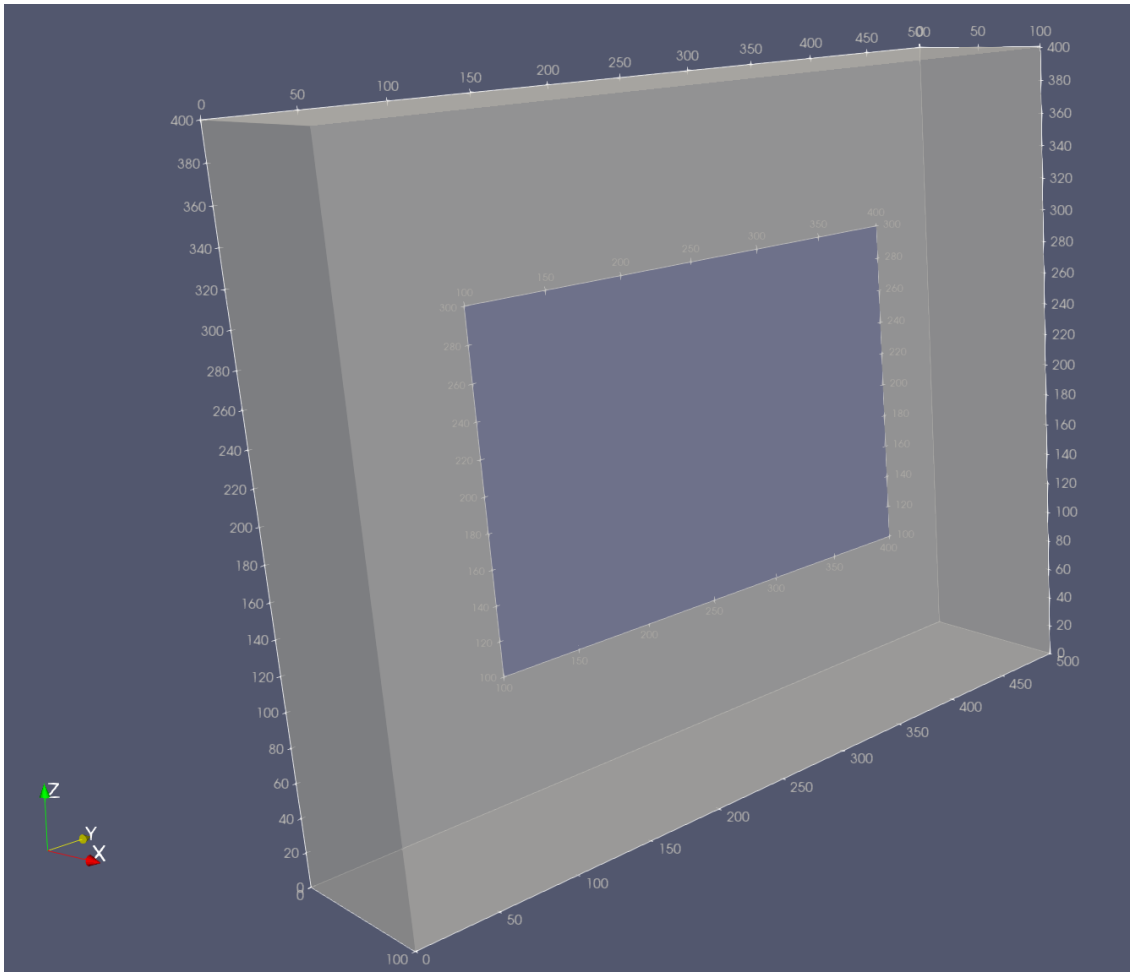

Figure 1: Geometry of the fracture embedded in the matrix domain.

Figure 2: Fracture cross-section showing high permeability unpropped channel occupying 10% of the total fracture height.

3.1 Bottom Injection, Bottom Production

The injector in this case is positioned at the bottom-left corner of the fracture, while the producer is located at the bottom-right. A low injection rate scenario is considered. The output temperature at the producer is tracked over a 10-year simulation period for four configurations: a base case with no high-conductivity channel, and cases with channel heights of 10%, 50%, and 90% of the total fracture height. Figure 3 illustrates the temperature evolution over time for each scenario.

The results reveal a significant thermal enhancement in the presence of a 10% channel, with the output temperature after 10 years approximately 15 °C higher than the base case. A 50% channel height yields an even greater increase of over 20 °C. However, further increasing the channel height to 90% diminishes this benefit, resulting in a temperature profile nearly identical to the base case.

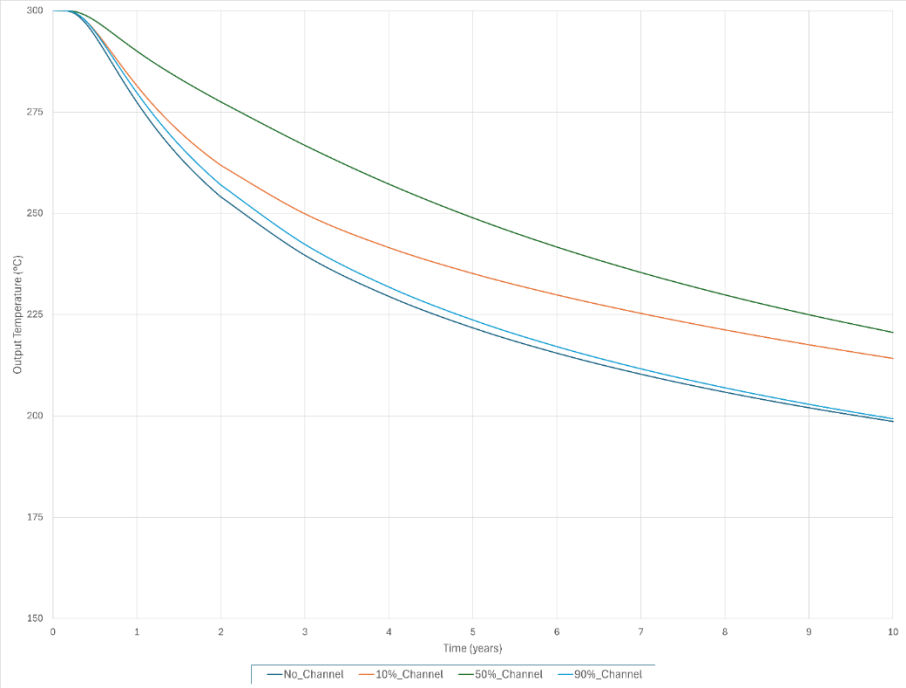

Figure 3: Output temperature at the producer over a 10-year simulation for Case 1, comparing the base fracture (no channel) with channel heights of 10%, 50%, and 90% of total fracture height under low injection rate conditions (bottom injection, bottom production).

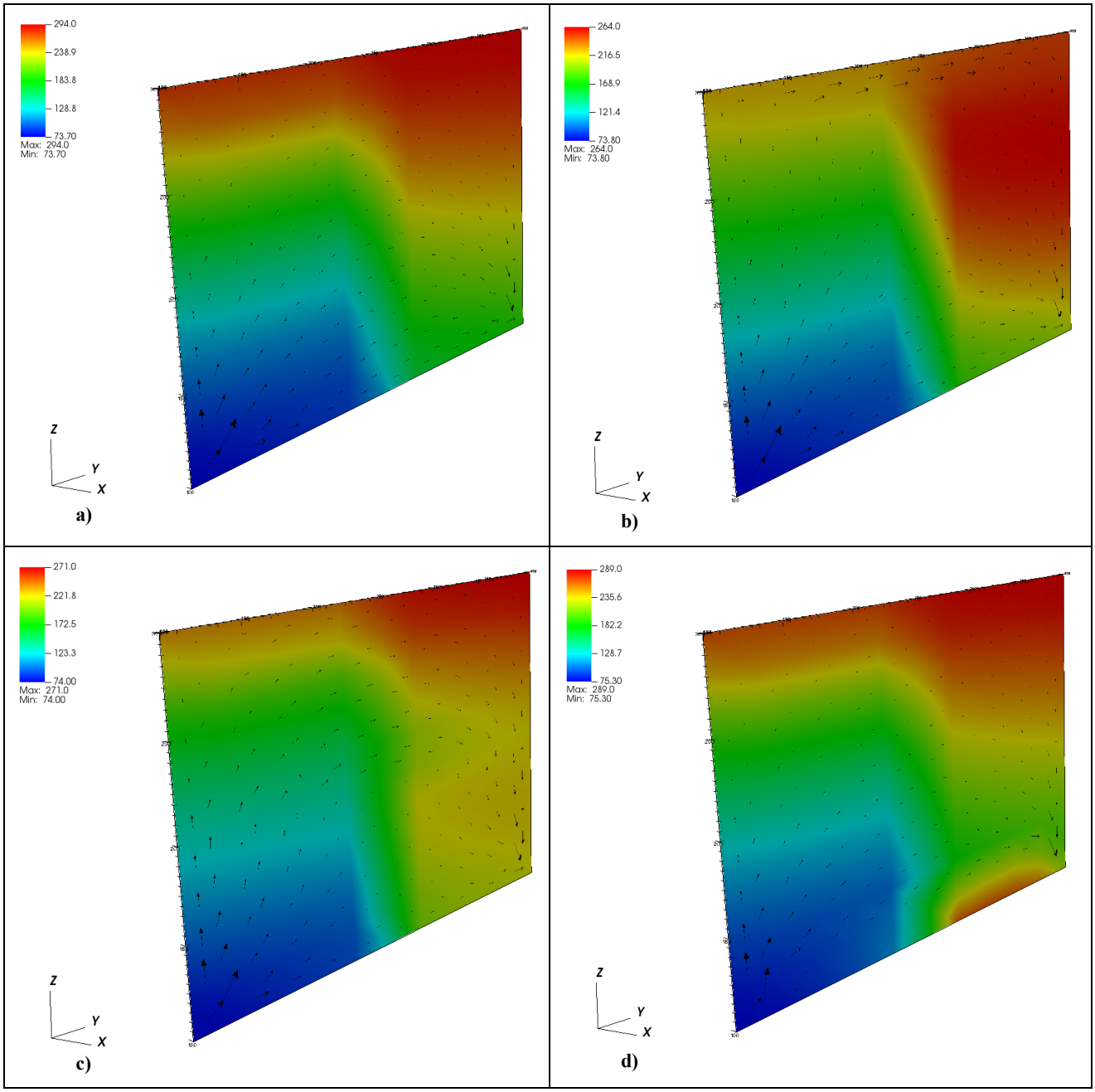

Figure 4: Temperature distribution and flow vectors along the fracture surface after 10 years of circulation for four channel configurations: (a) no channel, (b) 10% channel height, (c) 50% channel height, and (d) 90% channel height. Velocity vectors (black arrows) highlight preferential flow paths and their impact on thermal sweep efficiency under low injection rate (bottom injection, bottom production).

Figure 4 presents the temperature distribution along the fracture surface for the four scenarios described in Figure 3. In the base case without a high-conductivity channel, a substantial portion of the fracture retains its initial temperature of 300 °C after 10 years of circulation, explaining the lowest outlet temperature observed.

With a 10% channel height, the flow preferentially follows the high-conductivity path near the top of the fracture, as indicated by the velocity vectors in Figure 4b. This results in a noticeably higher outlet temperature compared to the base case. When the channel height increases to 50%, the cold injected water influences a larger portion of the fracture, leading to the most effective thermal sweep and the highest outlet temperature among all cases.

However, further increasing the channel height to 90% reduces thermal efficiency. The flow bypasses much of the fracture volume, favoring the upper region and leaving the lower 10%—which is less permeable—largely unaffected. This creates a dome-shaped zone near the producer that remains close to the initial temperature, as the flow tends to move vertically near the outlet and laterally away from the bottom region elsewhere. Consequently, the temperature profile in the 90% channel case resembles that of the base case.

To evaluate the impact of an increased injection rate, a rate of 500 m³/day was applied to the same four scenarios previously analyzed. Figure 5 illustrates how the output temperature evolves over the 10-year simulation period. Across all four cases, a substantial temperature decline—averaging around 50 °C—is evident.

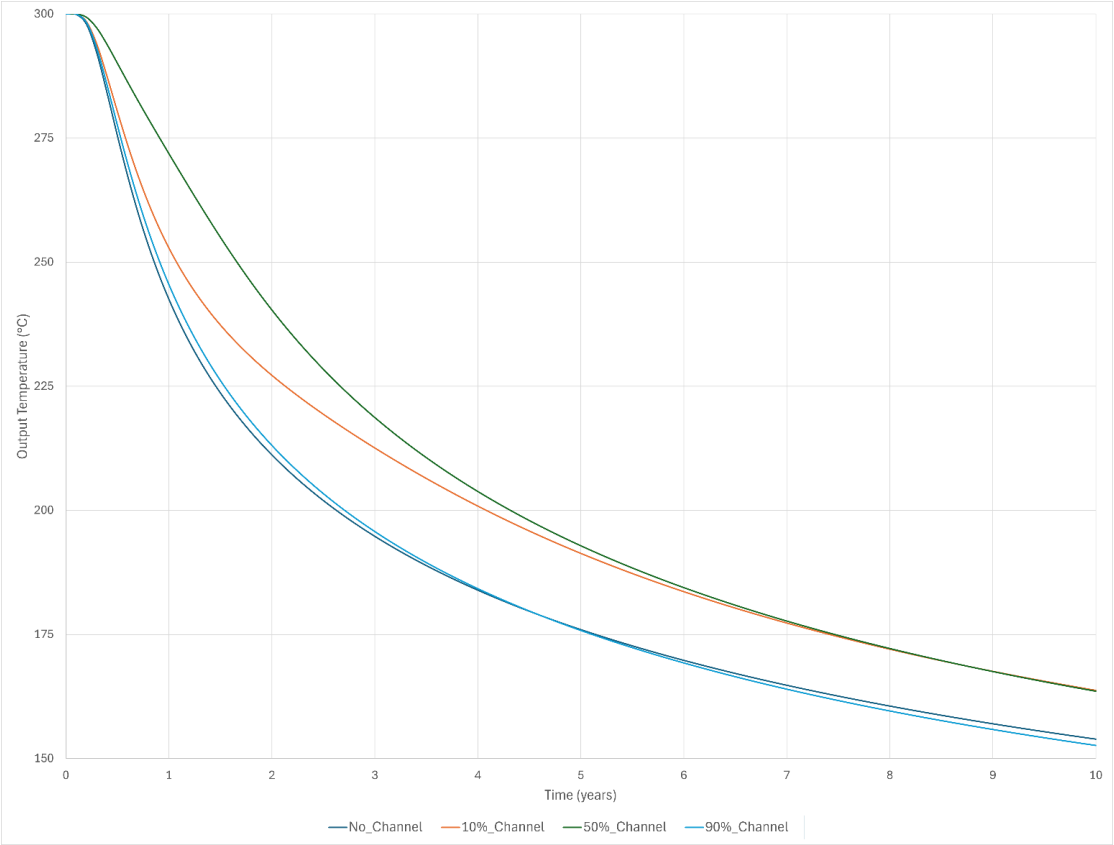

Figure 5: Output temperature at the producer over a 10-year simulation for Case 1, comparing the base fracture (no channel) with channel heights of 10%, 50%, and 90% of total fracture height under high injection rate conditions (bottom injection, bottom production).

Notably, the temperature difference between the 10% channel case and the base case without a channel narrows to less than 10 °C. Furthermore, after five years of continuous circulation, the 10% and 50% channel cases begin to follow a similar trend, while the base case and the 90% channel case also converge in behavior.

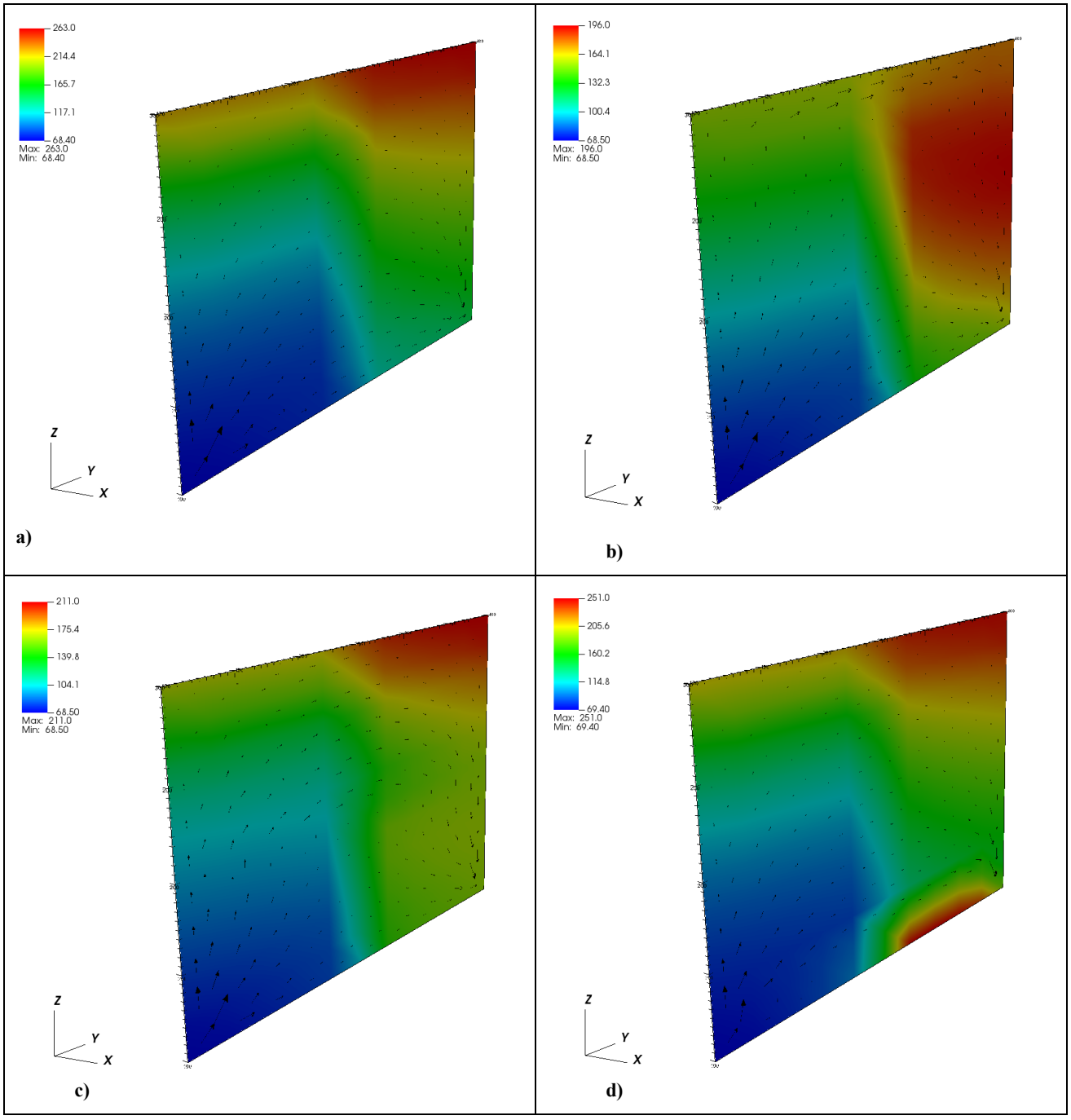

Figure 6: Temperature distribution and flow vectors along the fracture surface after 10 years of circulation for four channel configurations: (a) no channel, (b) 10% channel height, (c) 50% channel height, and (d) 90% channel height. Velocity vectors (black arrows) highlight preferential flow paths and their impact on thermal sweep efficiency under high injection rate (bottom injection, bottom production).

When comparing the temperature distribution across the fracture surface after 10 years of circulation to the previous lower injection rate scenario, a similar overall pattern emerges. The channeling effect remains pronounced in the 10% and 50% channel cases relative to the base case, while the dome-shaped thermal profile is still evident in the 90% channel configuration. One notable difference is the expansion of the cold region, which is significantly larger than in the lower injection rate scenario. The temperature distribution in the 50% channel case accounts for its superior output temperature during the first five years of circulation. Even after a decade, the 50% channel scenario consistently demonstrates the highest energy recovery from the rock matrix across the entire fracture surface. However, due to the increased injection rate, the fluid has less residence time to absorb heat from the rock, resulting in lower temperatures at the production well. Despite this limitation, incorporating channel structures into the simulation remains a critical factor in enhancing Enhanced Geothermal System (EGS) performance. For the specific injector-producer configuration examined here, channels up to 50% height offer clear benefits—though this advantage may not hold if the well placement is altered, as will be discussed later.

3.2 Middle Injection, Top Production

In this test case, the injector is positioned at the midpoint of the left boundary of the fracture, while the producer is located at the top right corner within the channel. The analysis focuses on a low injection rate scenario across four configurations: a fracture with no channel, and fractures with high-conductivity channels occupying 10%, 50%, and 90% of the total fracture height. Figure 7 illustrates the evolution of output temperature over a 10-year simulation period. Unlike previous configurations, omitting the channel in this setup leads to an overestimation of the output temperature by nearly 35 °C after 10 years, compared to the 10% channel case. This significant discrepancy underscores the critical role of incorporating high-conductivity channels in Enhanced Geothermal System (EGS) designs.

When the channel height is set to 50% of the fracture, the producer records a higher temperature during the first five years, indicating more efficient energy recovery relative to the 10% channel case. However, beyond the five-year mark, the temperature declines sharply, ultimately becoming the lowest among all four configurations. Increasing the channel height to 90% results in a temperature trend similar to the base case without a channel, though slightly lower by approximately 5 °C.

Figure 8 presents the temperature distribution along the fracture surface for each scenario. In the base case without a channel, the injected fluid effectively extracts heat from most of the fracture, except for the bottom right corner, which remains largely unaffected due to limited flow access caused by the producer's top-right location. Introducing a 10% channel shifts the preferential flow path to the uppermost portion of the fracture, as shown by the flow vectors in Figure 8b. Consequently, a substantial area of the fracture remains untouched by cold water even after 10 years, explaining the lower output temperature compared to the base case.

In the 50% channel scenario (Figure 8c), the entire lower half of the fracture retains its initial temperature, indicating minimal heat extraction from that region. This outcome aligns with the lowest recorded output temperature, as the injected fluid predominantly follows the upper channel path, bypassing the lower fracture zones. With the producer situated at the top, the fluid fails to reach deeper regions of the fracture. When the channel height is increased to 90%, the preferential flow path expands to encompass nearly the entire upper portion of the fracture. Figure 8d reveals a temperature distribution similar to the base case, except for a larger cold zone at the bottom. This similarity in output temperature between the base and 90% channel cases is attributed to the limited conductivity of the lower fracture region, which remains less influenced by the injected fluid compared to the highly conductive upper 90%.

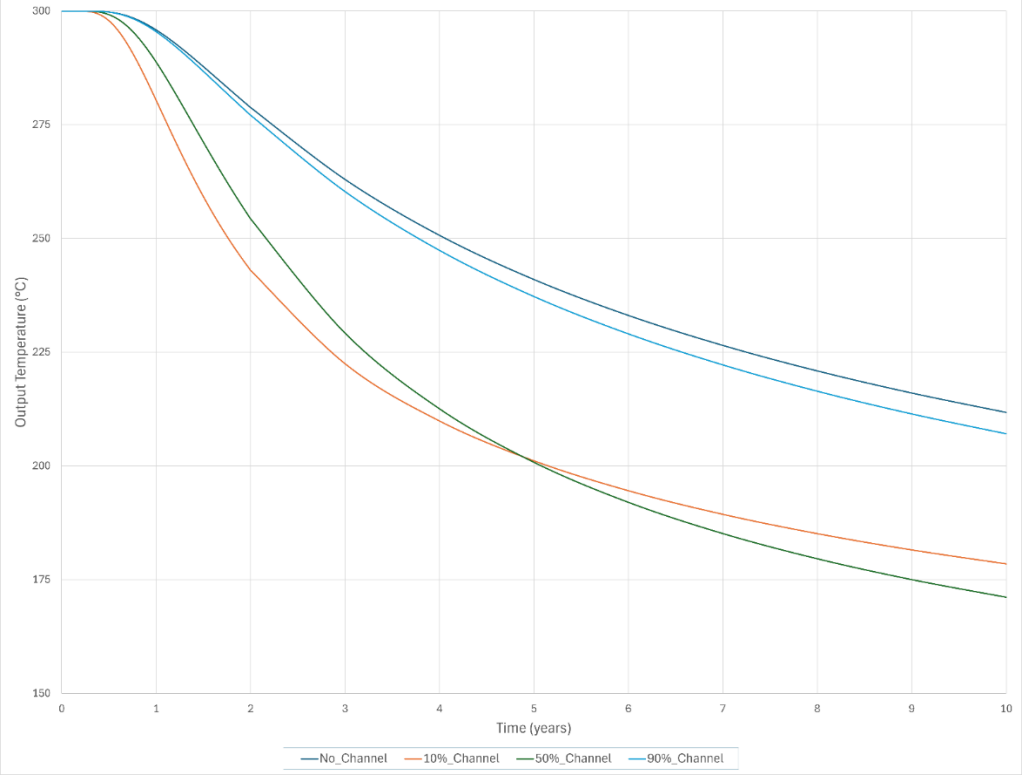

Figure 7: Output temperature at the producer over a 10-year simulation for Case 1, comparing the base fracture (no channel) with channel heights of 10%, 50%, and 90% of total fracture height under low injection rate conditions (middle injection, top production).

As in the previous test case, this scenario also examines the effect of a higher injection rate. Figure 9 presents the temperature variation over time for the four configurations: no channel, and channels occupying 10%, 50%, and 90% of the fracture height. The overall trends remain consistent with those observed under low injection rate conditions. However, two key observations emerge. First, the output temperature declines more rapidly, a direct consequence of the increased injection rate, which reduces the residence time of the fluid and

limits its ability to absorb thermal energy from the rock matrix. Second, the temperature gap between the 10% and 50% channel scenarios becomes more pronounced. This is due to a larger portion of the fracture surface remaining unaffected by the cold fluid, coupled with a higher energy recovery rate concentrated in the upper region of the fracture. As a result, the output temperature in the 50% channel case begins to drop below that of the 10% channel much earlier—around 1.75 years—compared to the five-year crossover point observed in the low injection rate scenario.

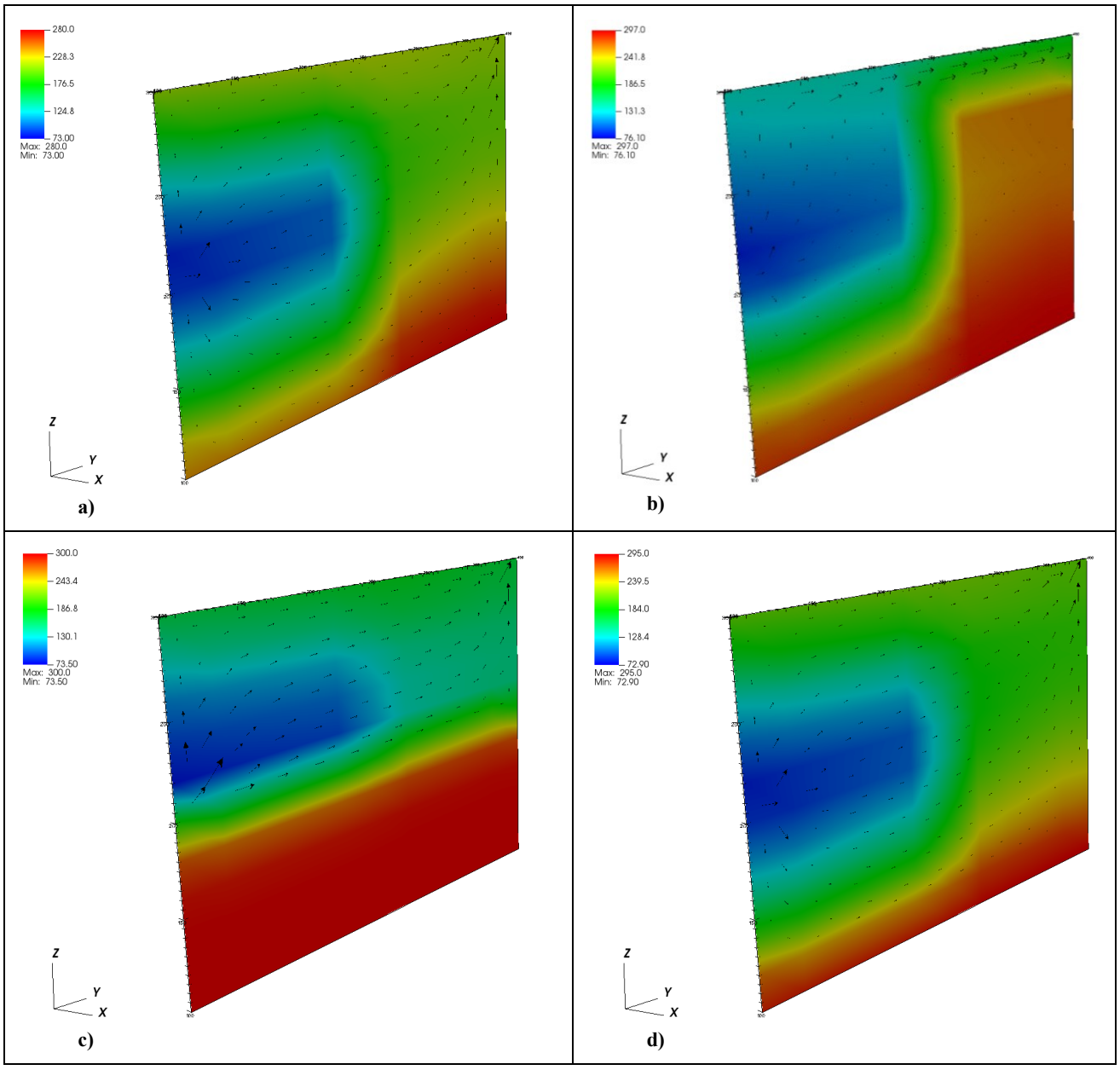

Figure 8: Temperature distribution and flow vectors along the fracture surface after 10 years of circulation for four channel configurations: (a) no channel, (b) 10% channel height, (c) 50% channel height, and (d) 90% channel height. Velocity vectors (black arrows) highlight preferential flow paths and their impact on thermal sweep efficiency under low injection rate (middle injection, top production).

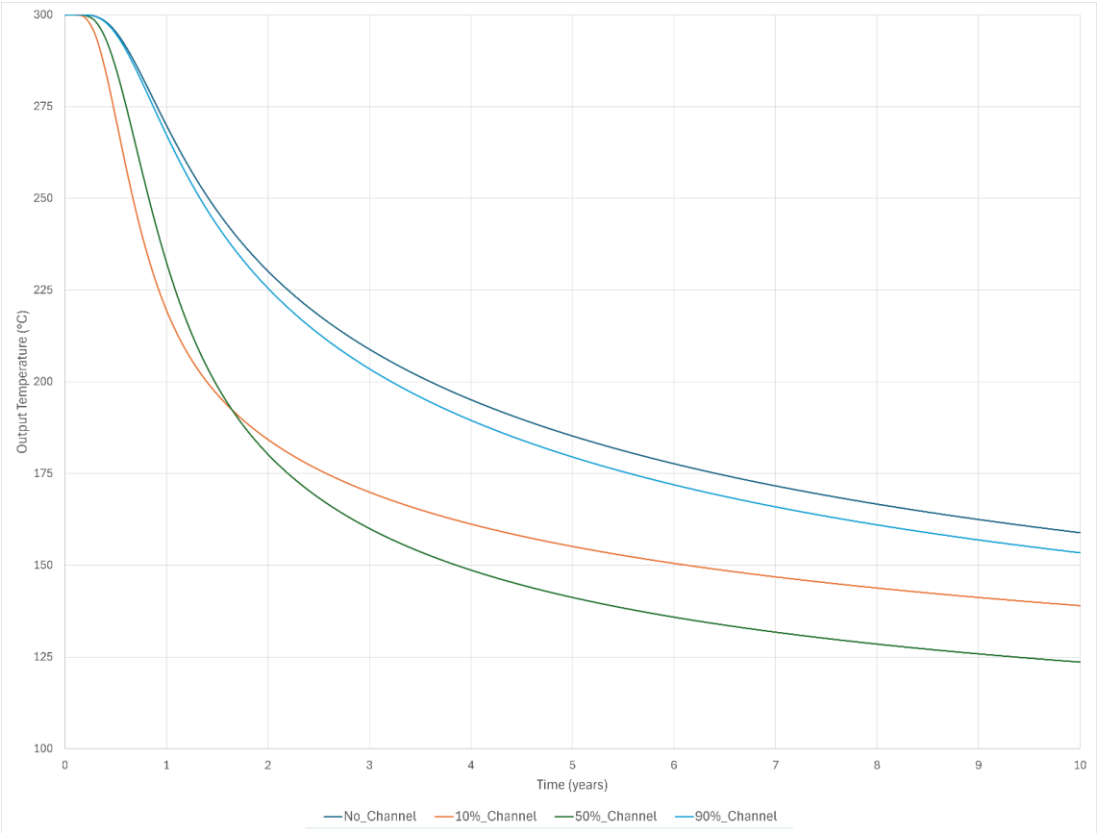

Figure 9: Output temperature at the producer over a 10-year simulation for Case 1, comparing the base fracture (no channel) with channel heights of 10%, 50%, and 90% of total fracture height under high injection rate conditions (middle injection, top production).

3.3 3D Surface Plot of Output Temperature

To investigate the combined influence of channel geometry and well placement on thermal performance, a series of simulations were conducted by systematically varying two parameters: the height of a high-conductivity channel within the fracture and the vertical depth offset between the injector and producer wells. In addition to the previously discussed cases, further simulations were performed with injector and producer locations varied between the bottom, middle, and top of the fracture. Each simulation setup incorporated four channel configurations: no channel, and channels occupying 10%, 50%, and 90% of the total fracture height. For reference, the output temperature profiles over time for all simulation cases are provided in the appendix.

For each configuration, the resulting output temperature was recorded. These data points were then used to construct a continuous surface representing output temperature as a function of the two input parameters. The resulting 3D visualization offers a comprehensive view of how variations in channel height and well depth offset interact to influence thermal recovery. The surface plot reveals key trends and sensitivities, providing valuable insight into optimal design strategies for enhanced geothermal systems.

To synthesize the results from all simulation scenarios, a surface plot was constructed using the output temperature normalized by the initial reservoir temperature. This normalization provides a measure of the energy sweeping efficiency relative to the reference rock temperature. The surface is plotted as a function of two key parameters: the fraction of the fracture height occupied by the high-conductivity channel, and the vertical depth difference between the producer and injector wells ($\Delta z = z_{producer} - z_{injector}$).

The purpose of this surface plot is to offer a rapid and intuitive assessment tool for estimating output temperature relative to reservoir temperature. It can be used to guide design decisions—such as selecting an appropriate channel height to meet a target output, optimizing well placement, or estimating performance based on existing configurations. While not intended as a precise predictive model, the plot serves as a practical reference for preliminary evaluations (Figure 10).

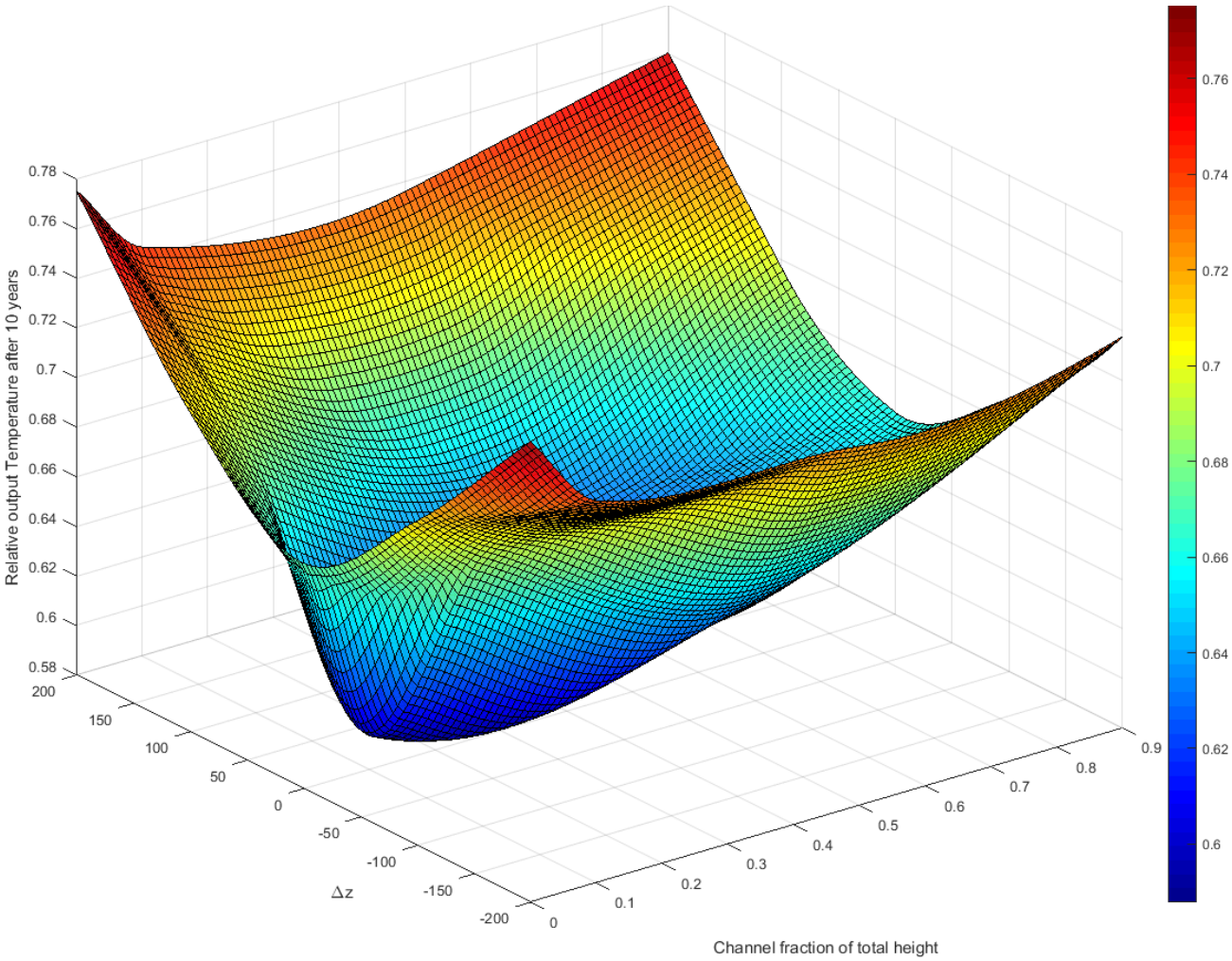

Figure 10: Normalized output temperature surface as a function of channel height fraction and vertical depth difference between injector and producer wells (Δz). The surface illustrates energy sweeping efficiency across all simulated scenarios (low injection rate).

To assess the impact of increased flow conditions, a similar analysis was performed for the high injection rate scenario. The resulting surface, shown in Figure 11, illustrates the normalized output temperature as a function of channel height fraction and vertical depth offset between the injector and producer wells.

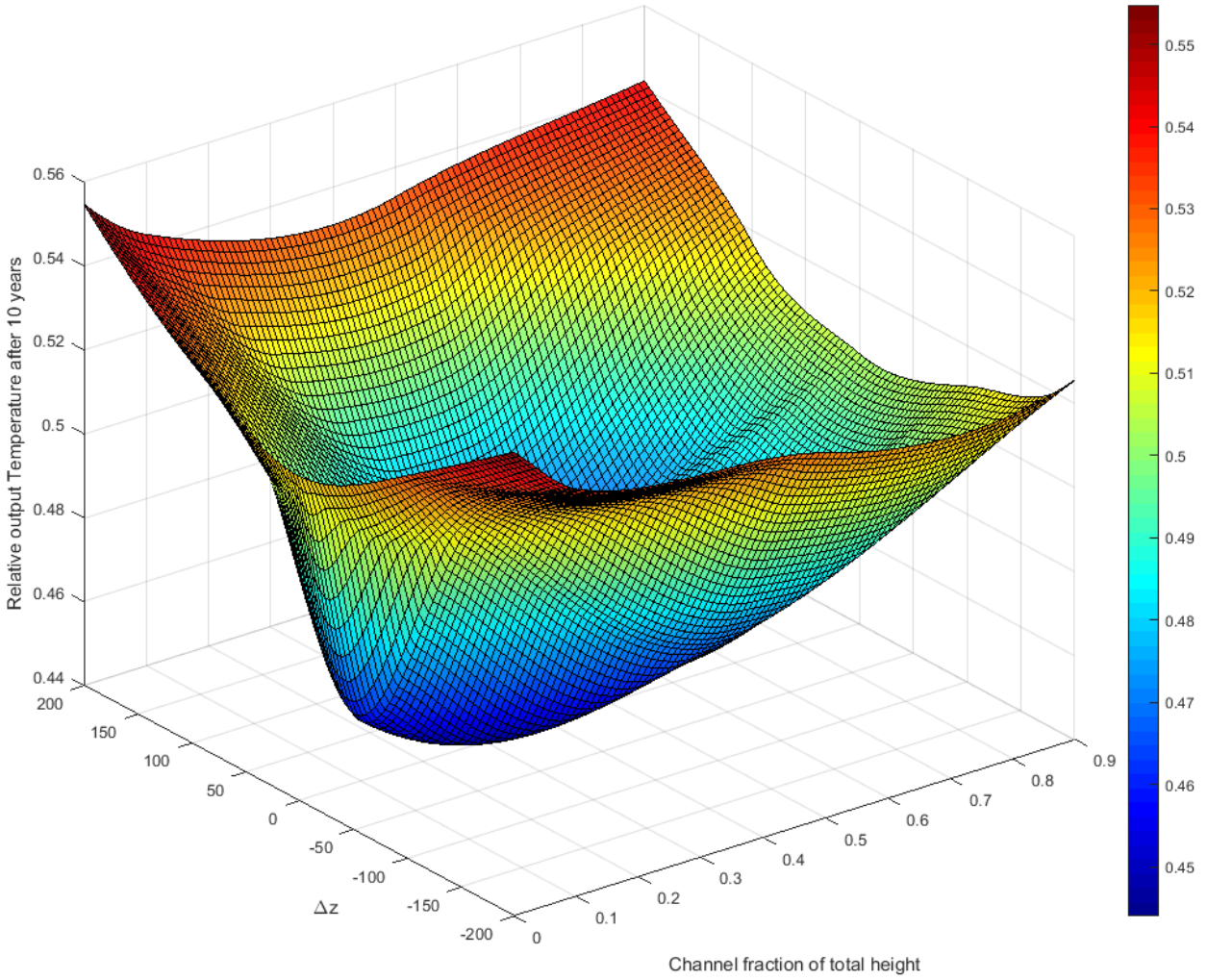

Figure 11: Normalized output temperature surface as a function of channel height fraction and vertical depth difference between injector and producer wells (Δz). The surface illustrates energy sweeping efficiency across all simulated scenarios (high injection rate).

4. CONCLUSION

This study highlights the critical influence of unpropped fracture segments—specifically high-conductivity channels—on thermal performance and well placement optimization in Enhanced Geothermal Systems (EGS). Through a series of simulations using the newly developed, in-house simulator, we explored how variations in channel height and vertical depth offset between injector and producer wells affect output temperature and energy recovery efficiency.

The results demonstrate that conductivity heterogeneity within fractures significantly alters subsurface flow dynamics and thermal behavior. Channels occupying up to 50% of the fracture height can enhance early-stage energy recovery but may also lead to premature thermal breakthrough if not paired with optimal well placement. The depth offset between wells further modulates these effects, emphasizing the need for integrated design strategies.

To synthesize these findings, a 3D surface plot was constructed to represent normalized output temperature as a function of channel height fraction and well depth difference. This visualization provides a practical tool for rapid assessment and preliminary design decisions.

By quantifying the operational significance of unpropped fracture zones and their interaction with well configurations, this work bridges a key gap in current modeling practices. It lays the groundwork for more accurate and adaptive EGS designs, with potential applications in real-time monitoring, control systems, and future field-scale implementations.

Future work will extend these simulations to explore additional geometric and hydraulic variations, including whether increased well spacing can mitigate early thermal breakthrough and whether such spacing remains practical at field scale. Moreover, the current study used a 1000× permeability contrast to isolate channel effects; upcoming analyses will examine whether channel height or permeability contrast is the dominant control on system performance.

REFERENCES

Alimahomed, N., Alimahomed, M., and Alimahomed, A.: Method for Enhancing Hydrocarbon Production Using Dual-Pack Proppant Placement, U.S. Patent No. 10,920,558 (2021).

Bertani, R.: Geothermal Power Generation in the World 2005–2010 Update Report, Geothermics, 41, (2012), 1–29.

Brown, D.W.: Hot Dry Rock Geothermal Energy: Important Lessons from Fenton Hill, Proceedings, 34th Workshop on Geothermal Reservoir Engineering, Stanford University, Stanford, CA (2009).

Jung, R.: EGS—Goodbye or Back to the Future, in Effective and Sustainable Hydraulic Fracturing, (2013), 95–121.

Liu, Y., Leung, J.Y., and Chalaturnyk, R.: Geomechanical Simulation of Partially Propped Fracture Closure and Its Implication for Water Flowback and Gas Production, SPE Reservoir Evaluation & Engineering, 21(2), (2018), 273–290.

Lund, J.W., Freeston, D.H., and Boyd, T.L.: Direct Utilization of Geothermal Energy: 2010 Worldwide Review, Geothermics, 40(3), (2011), 159–180.

Palisch, T.T., Vincent, M.C., and Handren, P.J.: Slickwater Fracturing: Food for Thought, SPE Production & Operations, 25(3), (2010), 327–344.

Samuel, M., Samuel, R., and Samuel, S.: System and Method for Enhancing Hydraulic Fracturing Using Heterogeneous Proppant Placement, U.S. Patent No. 7,451,812 (2008).

Tenma, N., Yamaguchi, T., and Zyvoloski, G.: The Hijiori Hot Dry Rock Test Site, Japan: Evaluation and Optimization of Heat Extraction from a Two-Layered Reservoir, Geothermics, 37(1), (2008), 19–52.

Wang, J., and Elsworth, D.: Role of Proppant Distribution on the Evolution of Hydraulic Fracture Conductivity, Journal of Petroleum Science and Engineering, 169, (2018), 377–388.

Warpinski, N.R.: Understanding the Mechanical Behavior of the Arch Region in Hydraulic Fractures, SPE Production & Operations, 24(3), (2009), 352–361.

Wu, W., and Sharma, M.M.: A Model for the Conductivity and Compliance of Unpropped and Natural Fractures, SPE Journal, 22, (2017), 1893–1914.

Zhang, H., Li, Y., and Zhao, J.: Influence of Arch Region on Fracture Transmissibility, Journal of Petroleum Science and Engineering, 165, (2018), 662–670.

Zhou, Y., Liu, Y., and Wang, Y.: Impact of Unpropped Fracture Conductivity on Gas Production Performance in Huff-n-Puff Operations, Journal of Petroleum Science and Engineering, 179, (2019), 106234.

Zimmerman, R.W., Kumar, S., and Bodvarsson, G.S.: Lubrication Theory Analysis of the Permeability of Rough-Walled Fractures, Int. J. Rock Mech. Min. Sci. & Geomech. Abstr., 28(4), (1991), 325–331

APPENDIX

This appendix contains the complete set of output temperature profiles for all simulation scenarios discussed in the main text. Each figure illustrates the temperature evolution over a 10-year circulation period, corresponding to different combinations of channel height fractions and well placement configurations. These plots serve as a reference for understanding the temporal behavior of each setup and support the analysis presented in the discussion and surface modeling sections.

Figures A1–A7 present the output temperature variations across four fracture configurations: no channel, and channels occupying 10%, 50%, and 90% of the total fracture height. These figures highlight the pronounced impact of well placement on thermal performance, with noticeable shifts in temperature profiles depending on the injector and producer locations. The results underscore the importance of accounting for the presence and geometry of high-conductivity channels when evaluating output temperature. In some cases, such as the scenario shown in Figure A1, neglecting the channel leads to a significant underestimation of the output temperature. In other configurations, the differences between scenarios are more subtle, as illustrated in Figure A2. However, in extreme cases—like that depicted in Figure A7—ignoring the channel effect can result in an overestimation of output temperature by as much as 100 °C, emphasizing the potential for substantial error in simplified models.

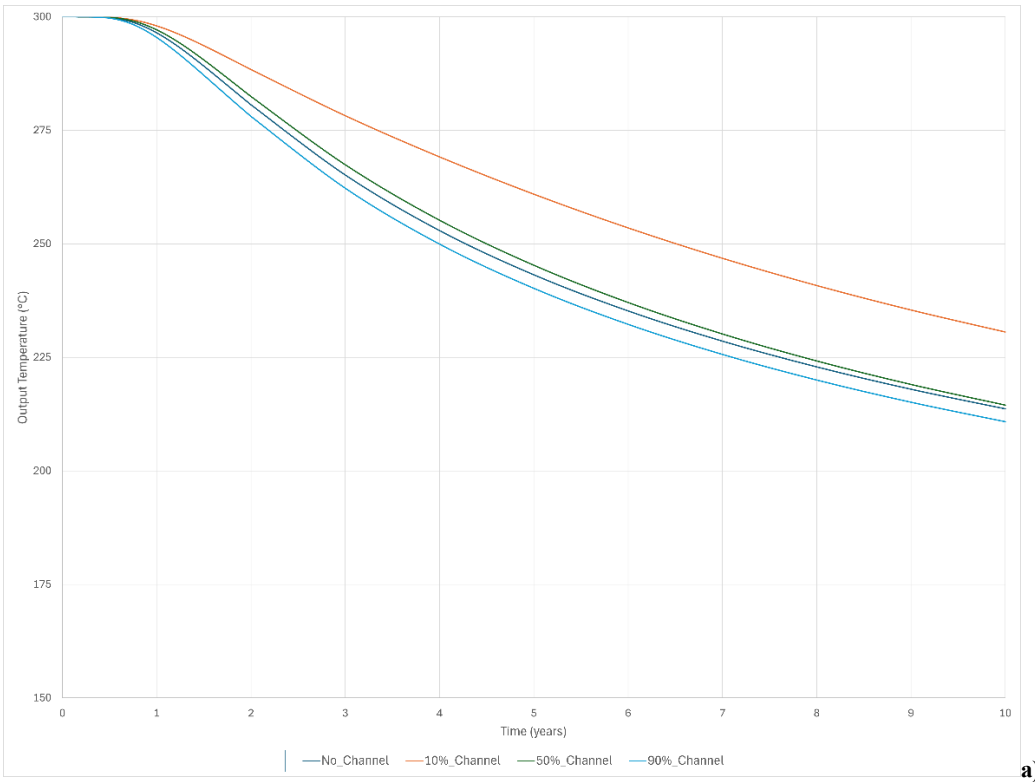

a)

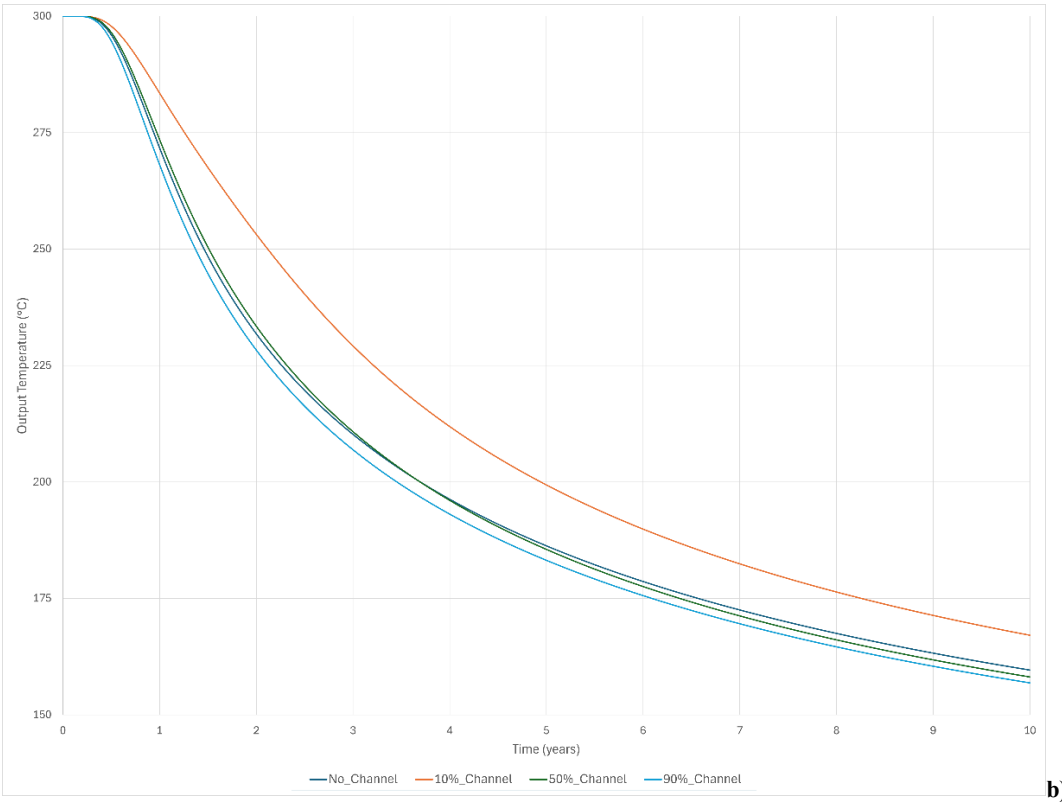

b)

Figure A1: Output temperature evolution over a 10-year circulation period for varying channel height fractions. Well placement configuration: bottom injection and middle production. Subfigures: (a) low injection rate, (b) high injection rate

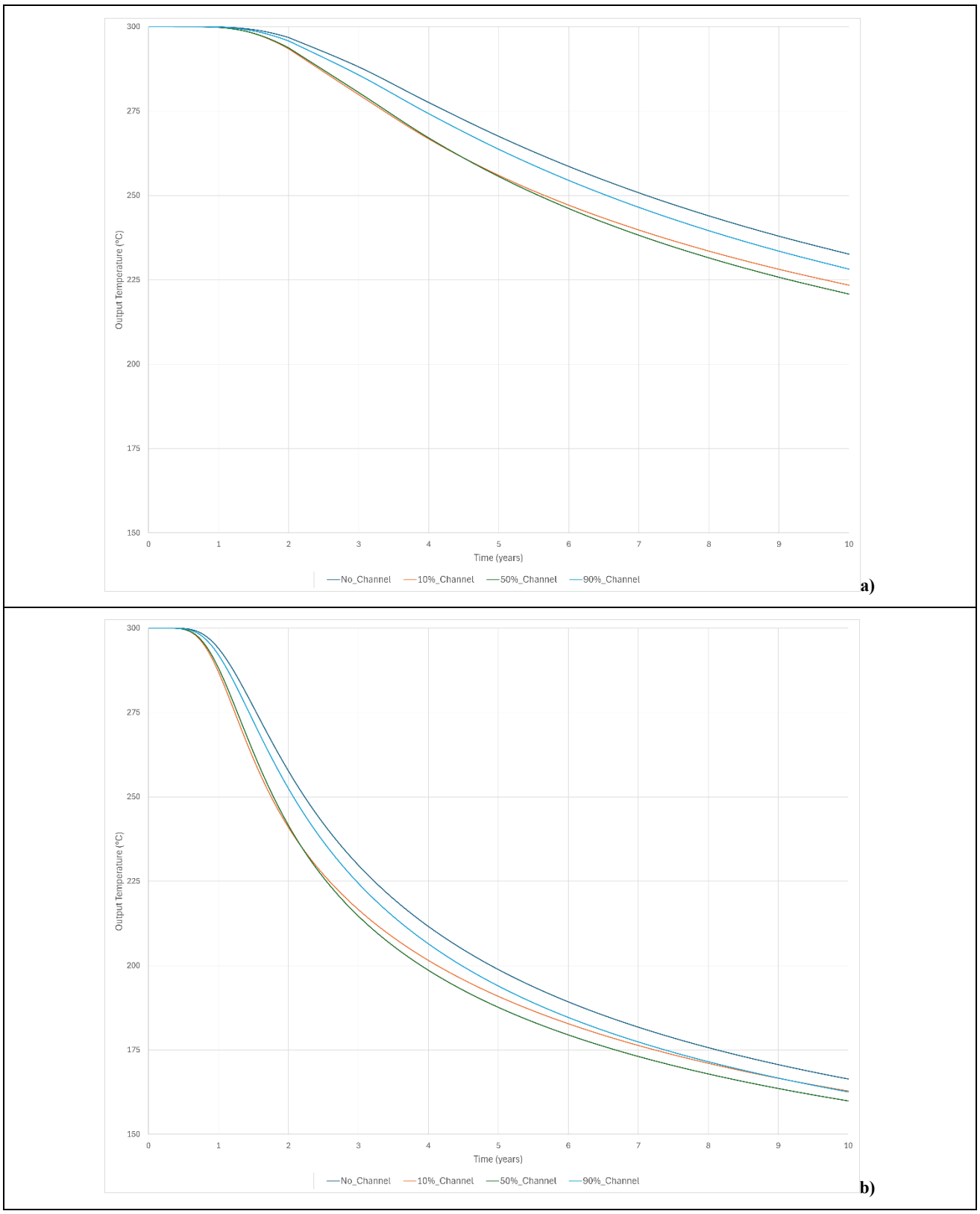

Figure A2: Output temperature evolution over a 10-year circulation period for varying channel height fractions. Well placement configuration: bottom injection and top production. Subfigures: (a) low injection rate, (b) high injection rate

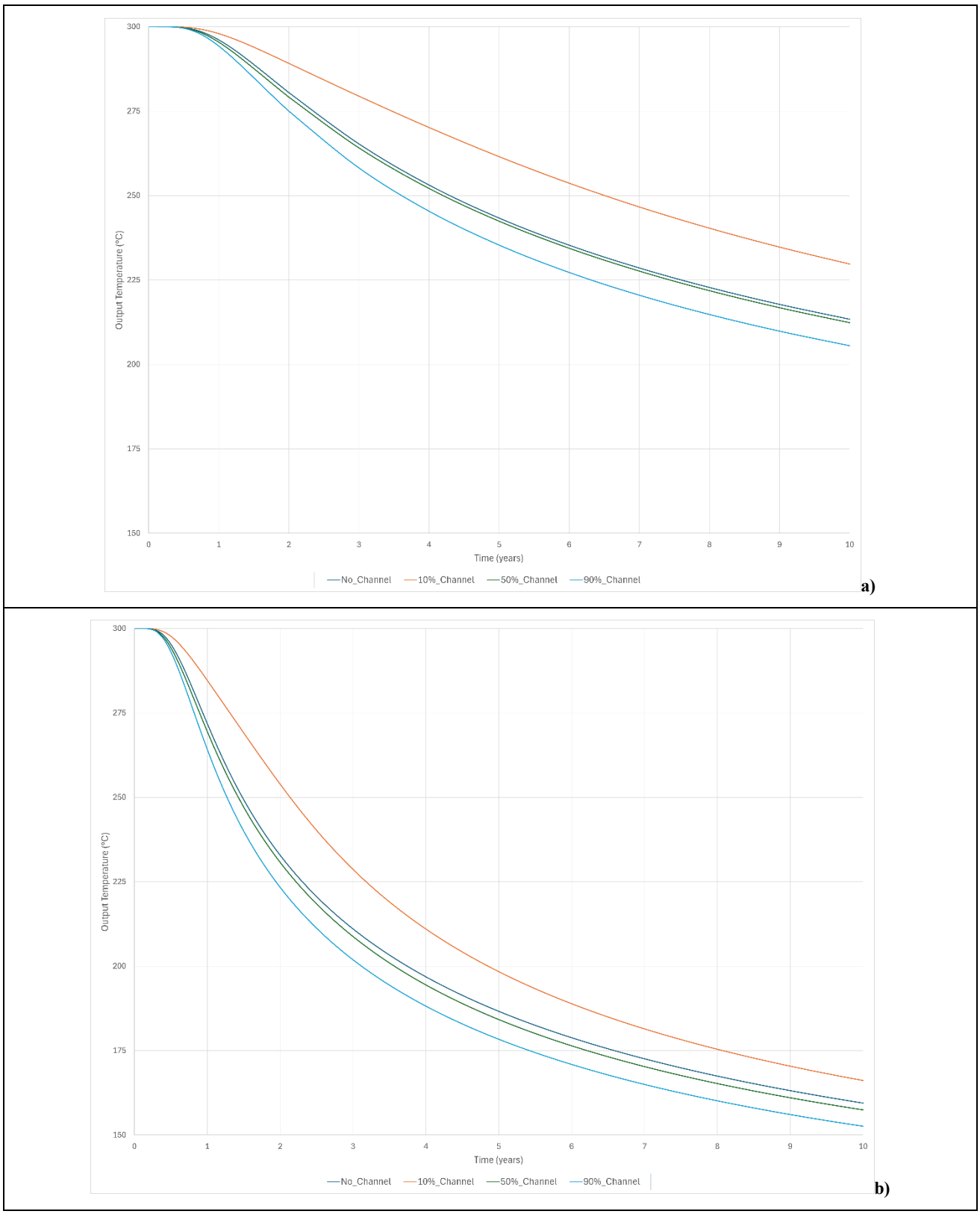

Figure A3: Output temperature evolution over a 10-year circulation period for varying channel height fractions. Well placement configuration: middle injection and bottom production. Subfigures: (a) low injection rate, (b) high injection rate

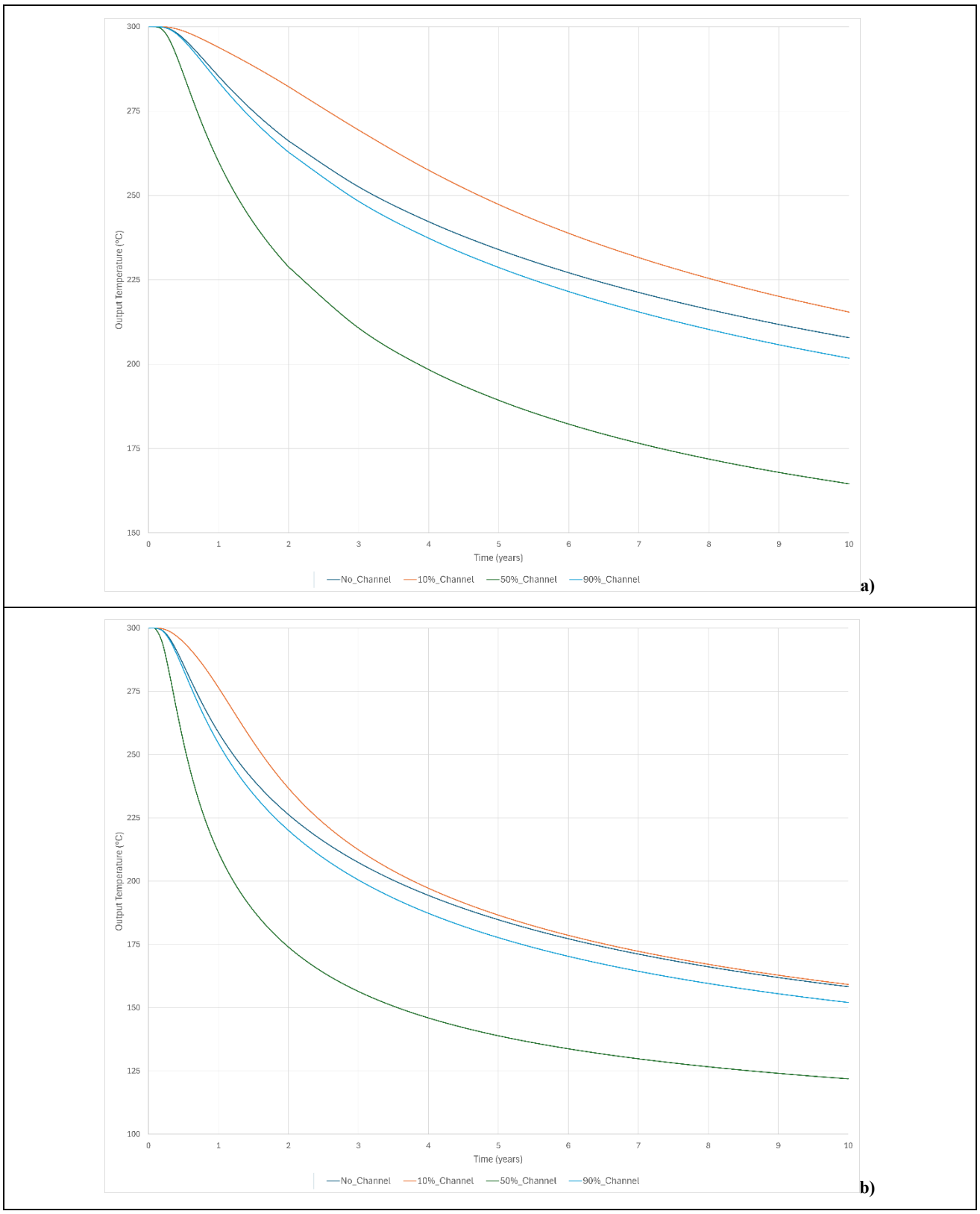

Figure A4: Output temperature evolution over a 10-year circulation period for varying channel height fractions. Well placement configuration: middle injection and middle production. Subfigures: (a) low injection rate, (b) high injection rate

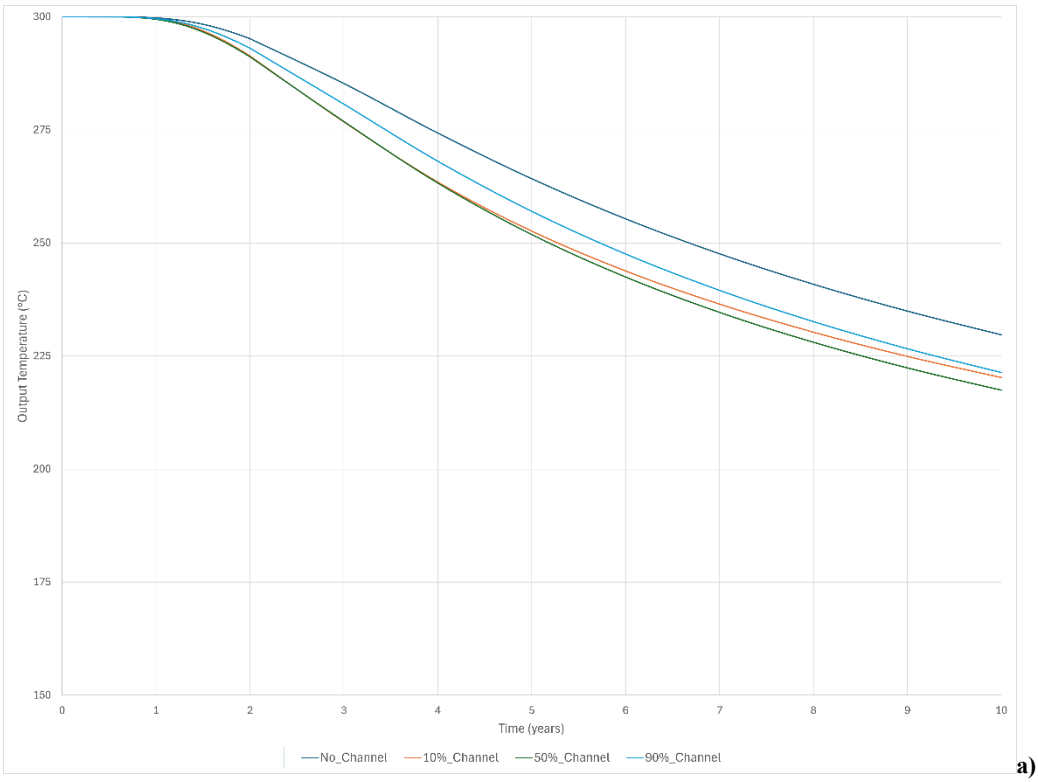

a)

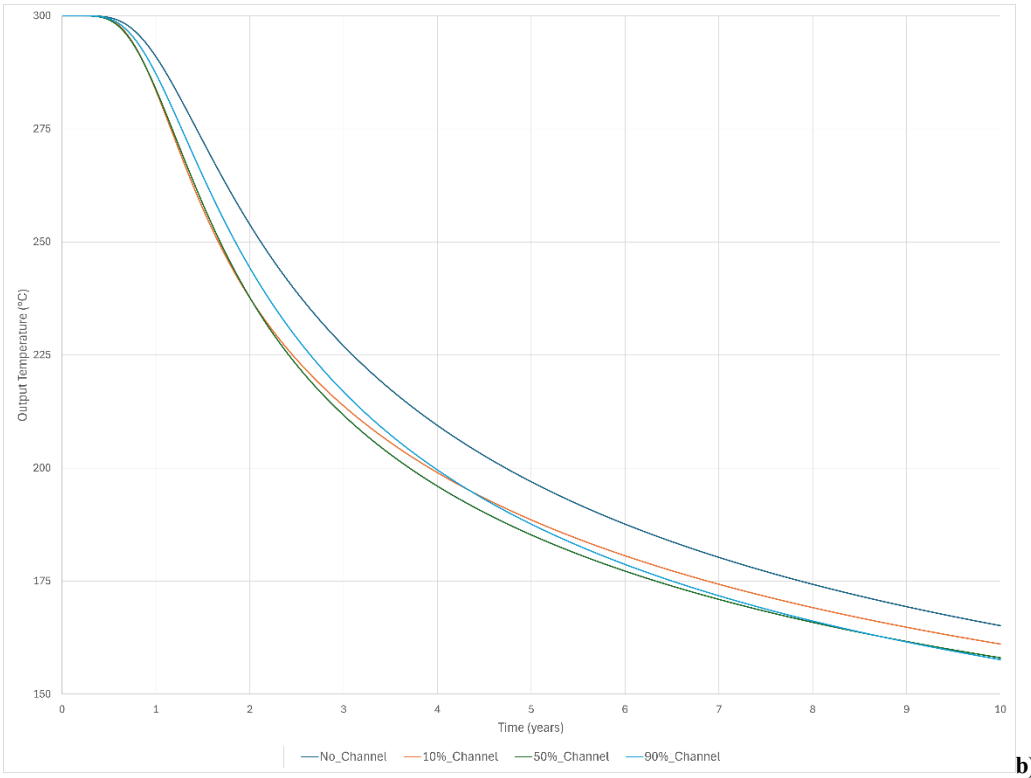

b)

Figure A5: Output temperature evolution over a 10-year circulation period for varying channel height fractions. Well placement configuration: top injection and bottom production. Subfigures: (a) low injection rate, (b) high injection rate

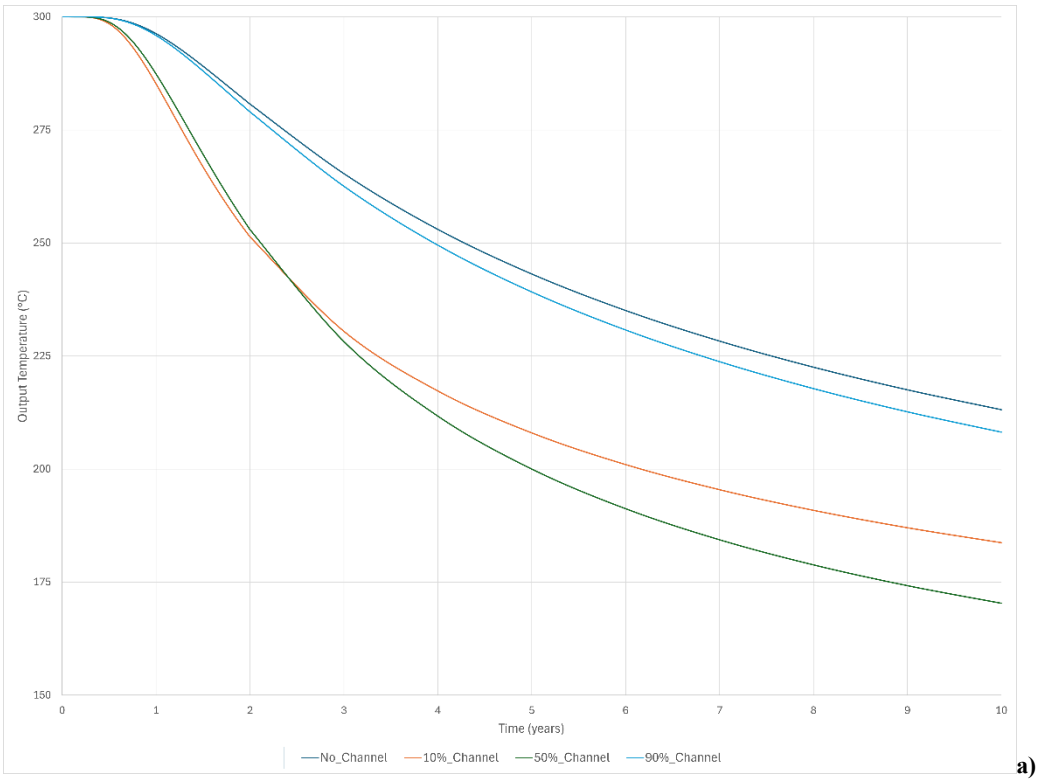

a)

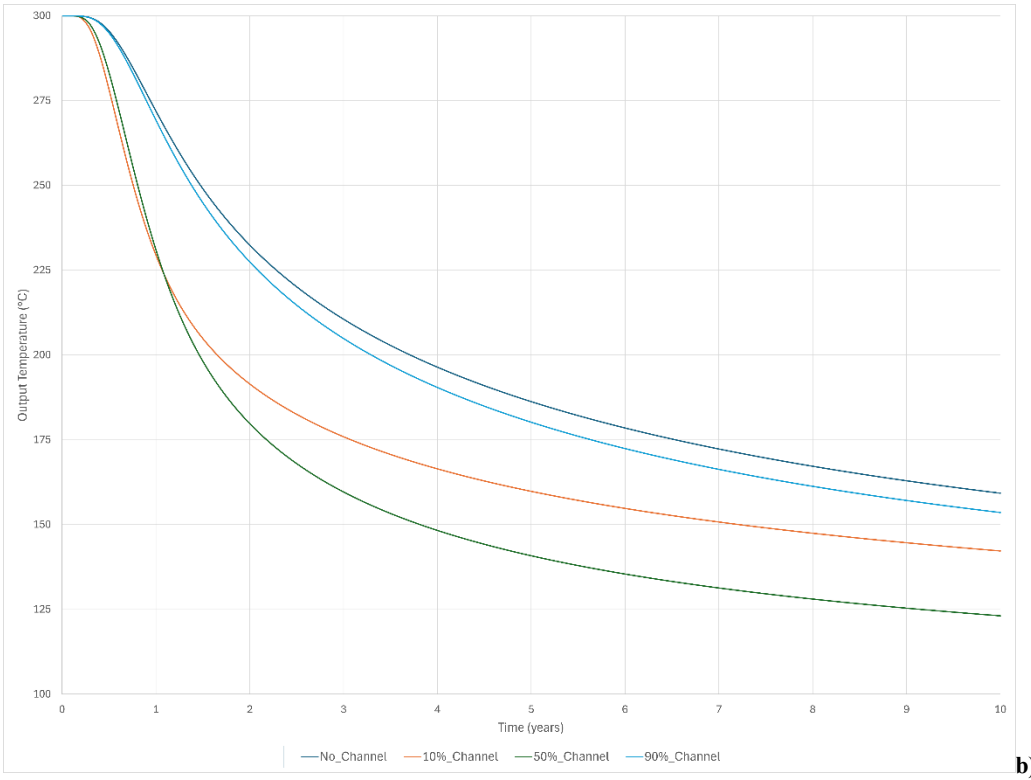

b)

Figure A6: Output temperature evolution over a 10-year circulation period for varying channel height fractions. Well placement configuration: top injection and middle production. Subfigures: (a) low injection rate, (b) high injection rate

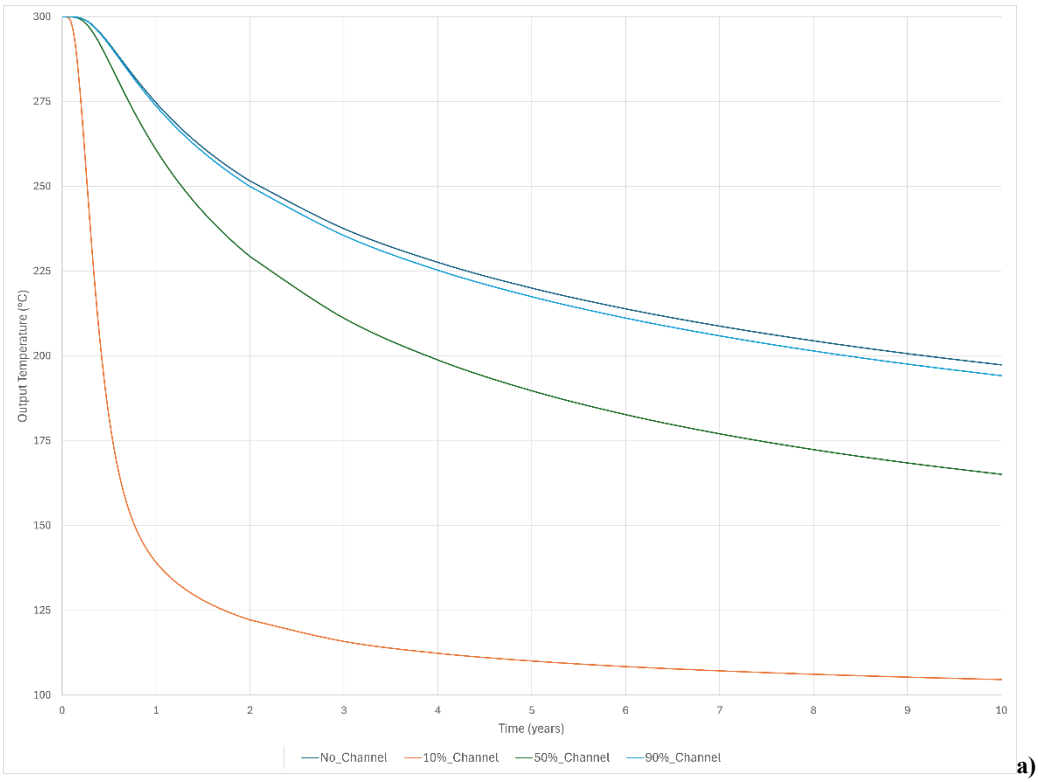

a)

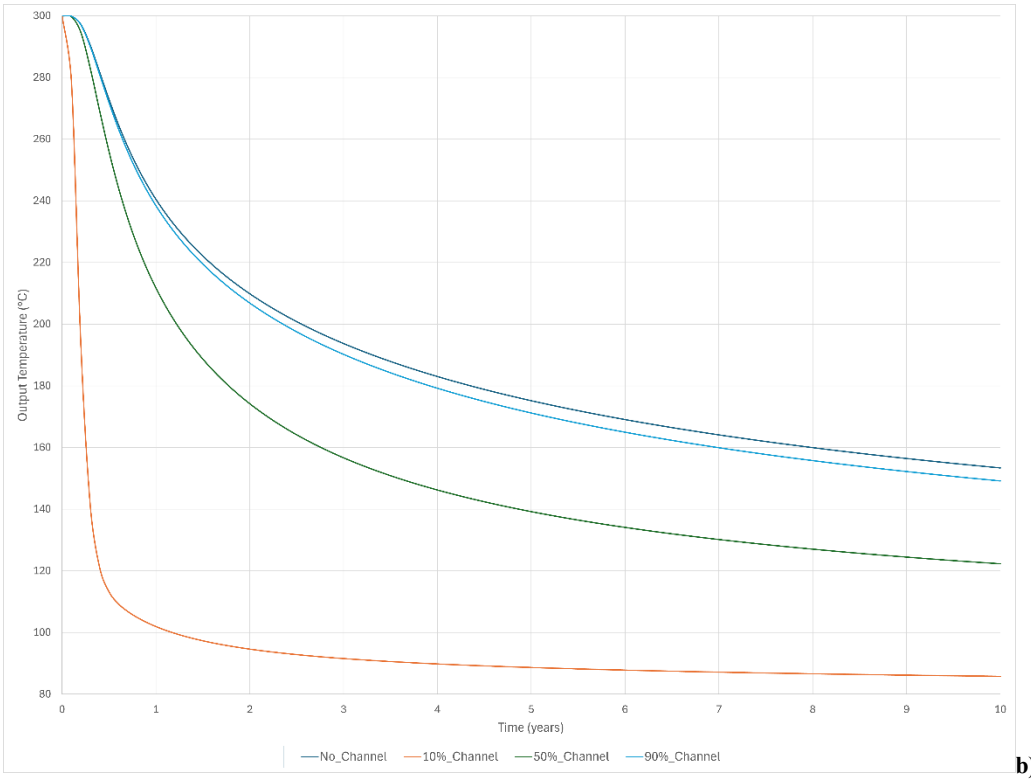

b)

Figure A7: Output temperature evolution over a 10-year circulation period for varying channel height fractions. Well placement configuration: top injection and top production. Subfigures: (a) low injection rate, (b) high injection rate